Challenges, myths, and opportunities of electron microscopy on halide perovskites 🔵✅

Special Collection: Hybrid Organic-Inorganic Halide Perovskites

Shulin Chen; Peng Gao ✉ 🆔

Check for updates

CrossMark

View Online

Export Citation

Articles You May Be Interested In

Transmission electron microscopy studies of organic–inorganic hybrid perovskites: Advances, challenges, and prospects

Applied Physics Reviews (June 2023)

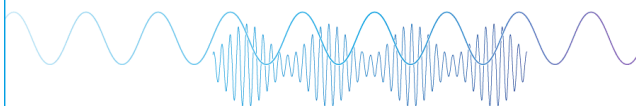A- or X-site mixture on mechanical properties of APbX_3 perovskite single crystals

APL Mater (April 2021)

Non-covalent interactions involving π effect between organic cations in low-dimensional organic/inorganic hybrid perovskites

Appl. Phys. Lett. (June 2023)

Challenges, myths, and opportunities of electron microscopy on halide perovskites ⓕ

View Online   Export Citation   CrossMark

Shulin Chen[1,2] and Peng Gao[1,3,a] (ID)

AFFILIATIONS

[1]International Center for Quantum Materials and Electron Microscopy Laboratory, School of Physics, Peking University, Beijing 100871, China
[2]State Key Laboratory of Advanced Welding and Joining, Harbin Institute of Technology, Harbin 150001, China
[3]Collaborative Innovation Center of Quantum Matter, Beijing 100871, China

Note: This paper is part of the special collection on Hybrid Organic-Inorganic Halide Perovskites
[a]**Author to whom correspondence should be addressed:** p-gao@pku.edu.cn

ABSTRACT

Organic–inorganic hybrid perovskites (OIHPs) have attracted extensive research interest as promising candidates for optoelectronic applications such as solar cells. Transmission electron microscopy (TEM)-based characterizations hold the key to revealing the morphological, microstructural, physical, and chemical information of OIHPs. However, their extreme sensitivity to the electron beam illumination usually inhibits us from obtaining the intrinsic information or even leads to significant artifacts. In this perspective, recent TEM studies on OIHPs are reviewed, wherein the discussions focus on how the electron beam destabilizes the structure of OIHPs and how to mitigate such effects as well as avoid misinterpretations. This perspective aims to catch researchers' attention on the beam sensitivity of OIHPs, guide the TEM characterization, and inspire electron microscopy development to reveal the working principle and failure mechanism of OIHPs.

05 September 2023 02:30:25

I. INTRODUCTION

Organic–inorganic hybrid perovskites (OIHPs) have attracted substantial research interest due to their great success in optoelectronic devices such as solar cells,[1,2] lasers,[3,4] and light-emitting diodes.[5,6] As a promising photovoltaic material, its power conversion efficiency rapidly increased from 3.8% initially[7] to 25.2% most recently,[8] which is comparable to the single-crystal silicon-based counterparts. Despite the great improvements, commercialization of this technology remains hindered by the instability of the materials.[9,10] It is because the weak hydrogen bonding or van der Waals forces in OIHPs makes them easy to decompose under a variety of environmental factors including heating,[11,12] exposure to oxygen[9] or moisture,[13] electrical bias,[14,15] UV light illumination,[16,17] and even electron beam irradiation.[18,19] These structural instabilities are closely related to electromigration, ion migration, and the interfacial relationship,[20,21] i.e., the ion migration induced by heating, electrical bias, and the light illumination can lead to the significant structural changes such as lattice distortion, interface failure, and material degradation, which further contributes to the hysteresis in

J–V curves and the poor long-term stability.[22,23] To solve the vital stability issue, it is of great importance to strengthen the fundamental understanding of the degradation mechanism, which can guide the rational device design and synthesis of OIHPs. Furthermore, improvements of the optoelectronic performance also rely on a better understanding about the structure–property relationships, i.e., how the microstructural features (including crystal defects, surface, and crystalline orientation) influence the macroscopic device performance.

Transmission electron microscopy (TEM)-based techniques that can achieve multiple-scale characterizations from micrometer to nanometer to the atomic scale contribute a lot to these fundamental understandings and the development of OIHPs-based solar cells.[24–26] Although various operation modes such as diffraction, imaging, and spectroscopy make TEM a powerful platform for characterizations, the concurrent inelastic events also inevitably bring in various damage effects to destabilize the structure. Considering the extreme sensitivity of the OIHP structure to the electron beam, such damage effects can be fatal sometimes. In some cases, the observed structural instability might come from the electron beam

illumination during characterizations instead of intrinsic information, unawareness of which could lead to incomplete or totally wrong conclusions. Fortunately, although the damage is unavoidable, its effect can be quantified to a certain degree and mitigated with careful control of the electron dose, from which a lot of useful information can be extracted to understand the intrinsic structure–property relationships and further guide the optimization of material synthesis and device fabrications.

In this perspective, we first briefly introduce the widely applied TEM techniques in characterizing OIHPs. Then, we show the extreme sensitivity of OIHPs to electron beam leads to the decomposition of $CH_3NH_3PbI_3$ (MAPbI$_3$) and $CH_3NH_3PbBr_3$ (MAPbBr$_3$). Importantly, we point out the mistakes in many literature studies that incorrectly identify PbI$_2$ as MAPbI$_3$ and show how to identify them correctly. Third, recent representative works that attempt to minimize the damage and achieve atomically resolved imaging are reviewed, and the effect of the accelerating voltage, temperature, crystalline facets, and coating on electron beam sensitivity is discussed. Finally, we summarize the earlier discussions into several directions and give our perspectives to this subject.

II. ELECTRON SCATTERING AND POSSIBLE DAMAGE

An electron scattering event can be either elastic or inelastic. In a TEM, when the incident high energy electrons interact with the thin TEM specimen, the scattered electrons carry abundant information of the targeting specimen, leading to a variety of operating modes by collecting different signals with different energy or momentum and bringing in comprehensive information about the phase, atomic structure, and chemical composition of the specimen (Fig. 1). For example, electron diffraction (ED), diffracting imaging, and high-resolution TEM (HRTEM) are produced by elastic scattering, while x-ray energy dispersive spectroscopy (EDS) and electron energy-loss spectroscopy (EELS) are associated with inelastic scattering.[27] Although we usually selectively collect one predominant type of scattered electrons to generate an image or a spectrum, it should be noted that elastic and inelastic scattering always co-exist regardless of the operating modes. During scattering, the incident electrons interact with the atoms of the specimen, making them vibrate, displace, or excite their inner shell electrons, leading to different types of possible beam damage during the TEM characterizations. The electron beam damage mechanism is complex and varies with materials, primarily including knock-on damage, radiolysis, and heating.[28,29]

Knock-on (displacement) damage is caused by the interaction between the incident electron and the atomic nucleus, which occurs when the transferred energy from the electron to the atomic nucleus exceeds the displacement energy threshold, generating interstitial atoms and vacancies. This damage is always observed in electrically conducting materials like metals and some semiconductors.[30] One common way of avoiding knock-on damage is to use a low energy incident electron beam below the threshold energy of materials. Radiolysis (ionization) damage mainly comes from the Coulomb interaction between the incoming electrons and the atomic electrons surrounding the nucleus. During radiolysis, several to hundreds of eV energy can be transferred to the atomic electrons by the incoming electrons, generating many holes in the
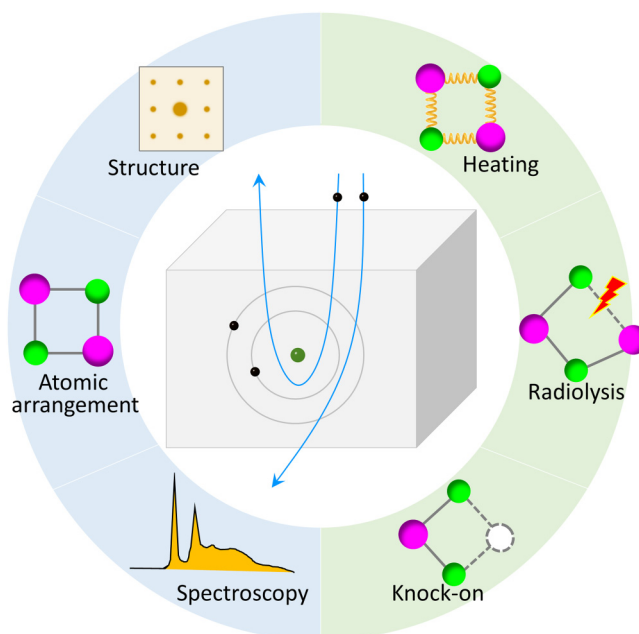

FIG. 1. TEM characterizations and inevitable electron beam damage effects.

valence band or inner shell and leading to the breakage of chemical bonds, the loss of crystallinity, and the escape of light atoms.[30] The transferred energy can further transfer to the atomic nuclei through phonons or excitons,[31] leading to the atomic displacement, as observed in polymers and alkali halides.[32] This damage mainly occurs in insulators and some semiconductors, because in the conducting specimen, the vacancies (holes) induced by the transferred energy can be rapidly filled by the electrons in the system.[30] For insulating polymers and biological materials with poor thermal conduction, phonon heating is the primary damage mechanism, wherein the incoming electrons excite the lattice vibration via loss of a small amount of energy. The temperature increase depends on the beam diameter, the beam current, thermal conductivity of the specimen, and the supporting grid. For example, the temperature rise is about 3 K for amorphous carbon with the current of 5 nA and a diameter of 0.2 nm.[29]

TEM-based techniques benefit the fundamental understanding of their intrinsic structure as well as the degradation mechanism for these fascinating solar cell materials, greatly contributing to the development of OIHPs-based solar cells.[24,25,33] At the same time, the beam damage is inevitable during the TEM characterizations, which is fatal for beam sensitive OIHPs. Therefore, it is essential to clarify how the electron beam impacts the structural instabilities and what factors influence the beam sensitivity and optimize the operating conditions to mitigate or avoid the damage for OIHPs.

III. TEM CHARACTERIZATIONS OF OIHPS

OIHPs have a general chemical formula of ABX$_3$, where A is the monovalent cation, such as methylammonium ($CH_3NH_3^+$) or

formamidinium [$HC(NH_2)_2^+$], B is bivalent metal cations like Pb^{2+} and Sn^{2+}, and X is a halogen ion (I^-, Cl^-, Br^-). In this perspective, we mainly focus on two typical materials: $MAPbI_3$ and $MAPbBr_3$. By operating under different modes, TEM characterizations deliver comprehensive structural and compositional information for OIHPs specimen, as shown in Fig. 2, including the micromorphology and size of the as-grown particles from the imaging and the crystallinity and lattice cell parameters [Figs. 2(a) and 2(b)] from the ED,[34,35] both of which are important to judge the specimen quality, thus guiding the material synthesis. It is well known that the single crystals show periodic diffraction reflections, while the polycrystals present diffraction rings and the amorphous materials demonstrate diffuse and weak diffraction rings. The HRTEM image can provide the lattice information, and the corresponding fast Fourier transform (FFT) pattern is useful to extract the crystalline information [Fig. 2(c)].[36] However, the contrast of HRTEM image relies on the specimen thickness, the defocus value of the objective lens, and the coefficient of spherical (Cs) aberration and thus is indirectly interpretable. EDS and EELS are spectroscopic techniques that can probe the chemical composition, the elemental distribution, chemical bonding, and the valence state [Figs. 2(d) and 2(e)].[36,37]

Besides these basic structural and chemical characterizations, recent advancements of *in situ* TEM enable the tracking of phase transformations at atomic and millisecond scales, providing unprecedented opportunities to probe the degradation mechanism of OIHPs under different external stimuli such as electrical bias and heating.[24] For example, by *in situ* high angle annular dark field (HAADF) scanning TEM (STEM) imaging techniques, Yang *et al.* found that vacuum itself is not likely to be responsible for the degradation since the formed Pb particles disappear during the prolonged preservation (30 days) in high vacuum conditions ($\sim 10^{-7}$ Torr) while heating to $\sim$50–60 °C causes a severe degradation, as shown in Fig. 2(f).[37] By using EDS techniques, Divitini *et al.* observed that the migration of iodine initiates at a low temperature (50–150 °C) while lead migrates at a high temperature above 175 °C [Fig. 2(g)].[38] By *in situ* HRTEM techniques, Kim *et al.* illustrate the details of thermally induced degradation process of $MAPbI_3$ and found that trigonal PbI_2 is precipitated from the amorphized $MAPbI_3$ layer via intermediated states.[39] Besides heating, Jeangros *et al.* also investigated the changes in the nanostructure of $MAPbI_3$-based solar cells under electrical bias and found that iodide migrates into a positively biased charge transport layer and volatilizes along with organic species, leading to the formation of PbI_2 and decreasing the cell performance [Fig. 2(h)].[14] Yuan *et al.* reported a reversible conversion between $MAPbI_3$ and PbI_2 under a small electric field at the elevated temperature at 330 K.[15]

Although these studies provide many valuable insights into the structure evolution and the degradation mechanism for OIHPs,[24] the electron dose information has been missing and the possible beam damage has been rarely discussed. It was reported that the high energy electron beam has already caused the degradation from $MAPbI_3$ to PbI_2 at small electron doses.[40] Considering that the *in situ* TEM experiments require additional time to control/adjust the imaging conditions, the beam damage should be much severer than conventional imaging. Thus it is worth

investigating whether or not *in situ* TEM experiments reveal the intrinsic structural instability, how the electron beam impacts the degradation, and what is the critical imaging condition for TEM characterizations of OIHPs.

IV. STRUCTURE SENSITIVITY TO THE ELECTRON BEAM AND THE DEGRADATION PATHWAY

Let us start the discussion with the ED technique that is widely used to extract the crystalline information of OIHPs. Compared to imaging and spectroscopy, the ED typically requires the lowest electron dose due to the parallel illumination of a large region. Thus, the possible electron damage can be minimized in the ED mode. However, substantial mismatches are observed between the experimental data and simulated ones of $MAPbI_3$, i.e., some of the diffraction spots are missing or weakened or additional spots appear, as shown in Fig. 3(a).[40] Further atomically resolved HAADF-STEM images verifying the formation of PbI_2 in Fig. 3(b)[40] account for these mismatches, indicating the degradation of $MAPbI_3$. Rothmann *et al.* noticed the extreme sensitivity to electron beam irradiation for $MAPbI_3$;[41] thus, they used a low dose rate (1 e Å^{-2} s^{-1}) with rapid acquisition conditions and successfully obtained the ED pattern of pristine $MAPbI_3$ as shown in Fig. 3(c). Furthermore, with appropriate dose minimization techniques, they again acquired the ED pattern from pristine tetragonal $MAPbI_3$, as shown in Fig. 3(d).[42] After 1 min irradiation at a dose of 100 e Å^{-2}, additional diffraction spots that are forbidden in tetragonal $MAPbI_3$ appear due to the structural and chemical changes. They proposed that a new intermediated phase is formed under the electron beam irradiation, possibly caused by the octahedral tilts or rotations. With increased dose, the intensities of some diffraction reflections decrease and finally disappear due to the beam damage. Rothmann's studies suggested that OIHPs can be easily damaged and the critical dose to obtain the pristine OIHPs structure is quite low.

In order to reveal the decomposition pathway, Chen *et al.* tracked the structure evolutions of single-crystal $MAPbI_3$ by using the controlled low-dose ED technique.[40] At a dose rate of 1 e Å^{-2} s^{-1}, the obtained ED [Fig. 4(a)] pattern is consistent with the simulated one of tetragonal $MAPbI_3$ [Fig. 4(e)]. Similar to Rothmann's observation, with increased doses, additional superstructure spots are observed [Fig. 4(b)]. Although both the octahedral tilts[43] and ordered vacancies[40] can cause superstructure diffraction reflections in perovskite oxides, for $MAPbI_3$, they interpret such a superstructure by ordered vacancies, since OIHPs are prone to lose negatively charged halide ions under the electron beam.[29] The structure with ordered iodine vacancies ($MAPbI_{2.5}$) is shown in Fig. 4(j), whose simulated ED pattern [Fig. 4(f)] matches the experimental one [Fig. 4(b)]. Moreover, such an intermediated superstructure has also been observed in $MAPbBr_3$ and inorganic perovskites ($CsPbBr_3$),[44] suggesting that vacancies in the form of $ABO_{2.5}$ are more general in OIHPs and their all-inorganic counterparts rather than an exception in $MAPbI_3$, similar to those observed in perovskite oxides in the form of $ABO_{2.5}$. With increased doses, the structure keeps losing MA and the rest of the I ions to form $MA_yPbI_{2.5-z}$ ($0 \leq y \leq 1$ and $0 \leq z \leq 0.5$)
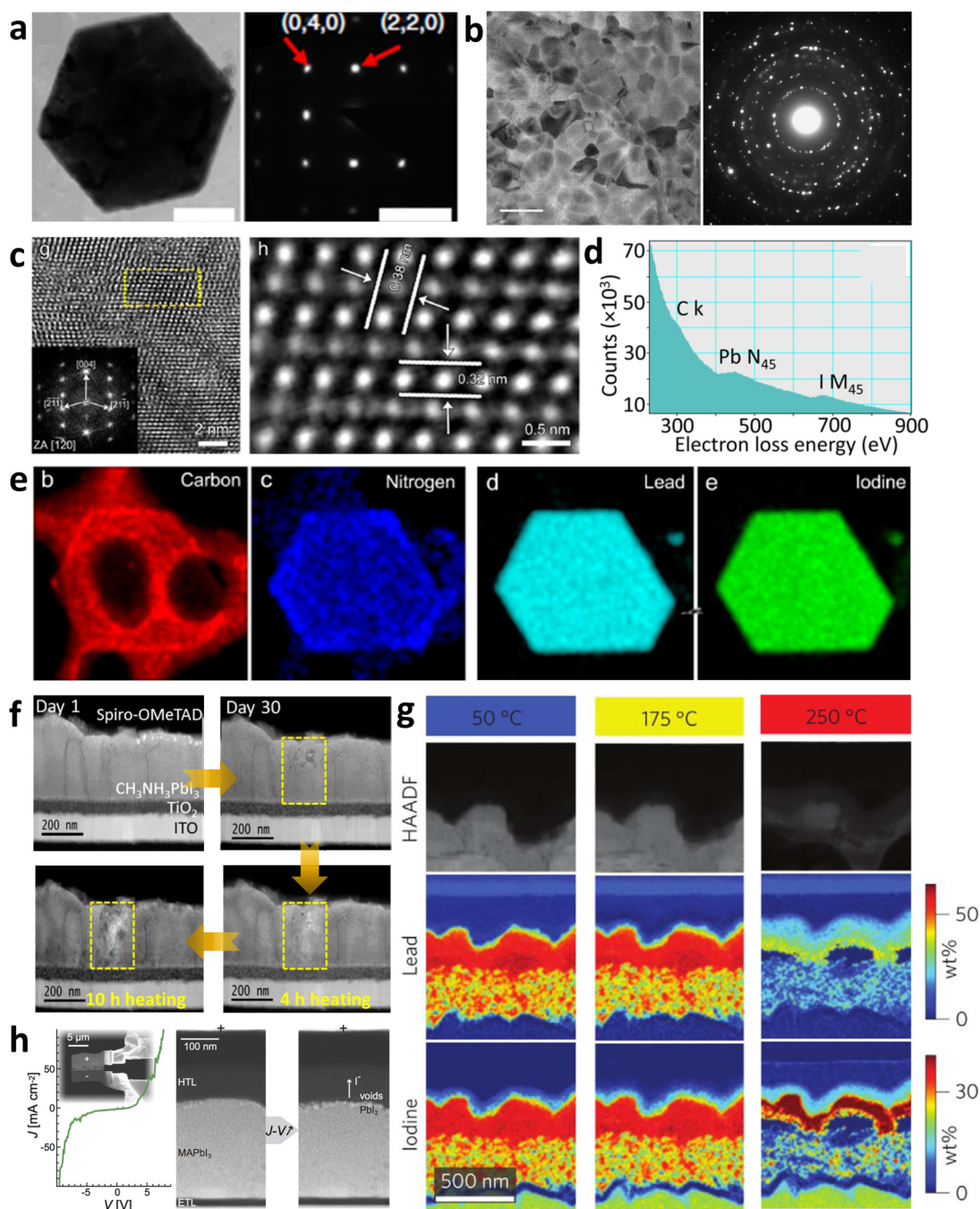
FIG. 2. TEM characterizations and *in situ* TEM studies of MAPbI₃. (a) and (b) TEM images and ED patterns of single-crystal and polycrystal MAPbI₃. Images are reproduced with permission from Li *et al.*, Nat. Commun. **7**, 11330 (2016). Copyright 2016 Nature Publishing Group; and Alberti *et al.*, Nat. Commun. **10**, 2196 (2019). Copyright 2019 Nature Publishing Group. (c) HRTEM image and the corresponding FFT pattern. (d) EELS spectrum and (e) EDS mapping. The images in (c) and (e) are reproduced with permission from Niu *et al.*, Adv. Mater. **27**, 7800–7808 (2015). Copyright 2015 Wiley-VCH. (f) Real-time cross-sectional HAADF images of a typical perovskite solar cell device under a high vacuum condition (~10⁻⁷ Torr) for 30 days and then heating. The pictures in (d) and (f) are reproduced with permission from Yang *et al.*, ACS Appl. Mater. Interfaces **8**, 32333–32340 (2016). Copyright 2016 American Chemical Society. (g) HAADF and the corresponding EDS mapping to show the migration of Pb and I with increased temperature. Reproduced with permission from Divitini *et al.*, Nat. Energy **1**, 15012 (2016). Copyright 2016 Nature Publishing Group. (h) The iodine migration under the electrical bias. Reproduced with permission from Jeangros *et al.*, Nano Lett. **16**, 7013–7018 (2016). Copyright 2016 American Chemical Society.
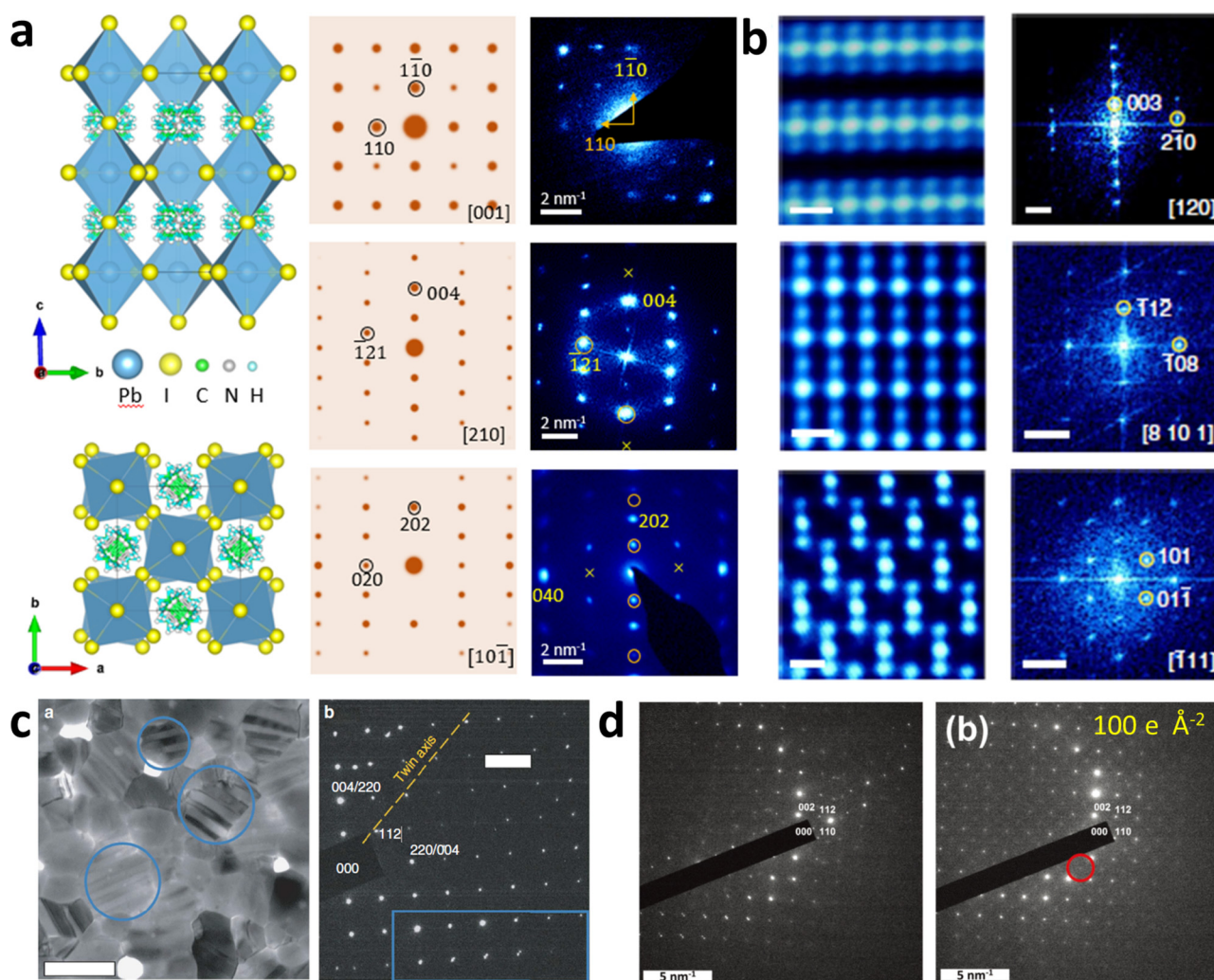
FIG. 3. ED characterizations of MAPbI$_3$ structure. (a) The mismatches between the simulated and experimental ED patterns of MAPbI$_3$ and the corresponding atomistic structures. (b) The atomically resolved HAADF-STEM images of PbI$_2$ along different viewing directions. The images in (a) and (b) are reproduced with permission from Chen *et al.*, Nat. Commun. **9**, 4807 (2018). Copyright 2018 Nature Publishing Group. (c) TEM image and the corresponding ED pattern from the pristine MAPbI$_3$ at a low dose rate of 1 e Å^{-2} s^{-1}. Reproduced with permission from Rothmann *et al.*, Nat. Commun. **8**, 14547 (2017). Copyright 2017 Nature Publishing Group. (d) ED patterns from pristine MAPbI$_3$ to an intermediated phase with additional reflections. Reproduced with permission from Rothmann *et al.*, Adv. Mater. **30**, 1800629 (2018). Copyright 2018 Wiley-VCH.

[Figs. 4(c), 4(g), and 4(k)]. Finally, the perovskite structure framework collapses and transforms into layered PbI$_2$ phase [Figs. 4(d), 4(h), and 4(l)]. Such a degradation pathway has also been observed in MAPbBr$_3$, suggesting that the decomposition of OIHPs, regardless of being cubic or tetragonal, starts with the loss of ordered halogen ions, followed by the loss of remaining halogen and methylamine ions, leading to eventual crumble of perovskite framework and decomposition into PbX$_2$.[44]

Note that pristine MAPbI$_3$, intermediate phase, and final product PbI$_2$ share similar ED patterns with similar symmetry and lattice parameters judging from the primary Bragg reflections

(Fig. 4), although the relative intensity of different reflections changes dramatically. In fact, such a case with only changes in relative intensity while the overall symmetry remains similar can be easily confused especially for non-specialists in crystallography, because extinction (forbidden reflections) and double diffraction (multiple scattering) that commonly occur in the ED can lead to the same phenomena. Therefore, in many previous studies,[35,45–64] such inconsistent ED patterns were largely ignored and incorrectly identified (Table I), and the electron beam induced damage during the TEM characterizations has been rarely discussed. To avoid such mistakes in future, we have compared the differences in structure
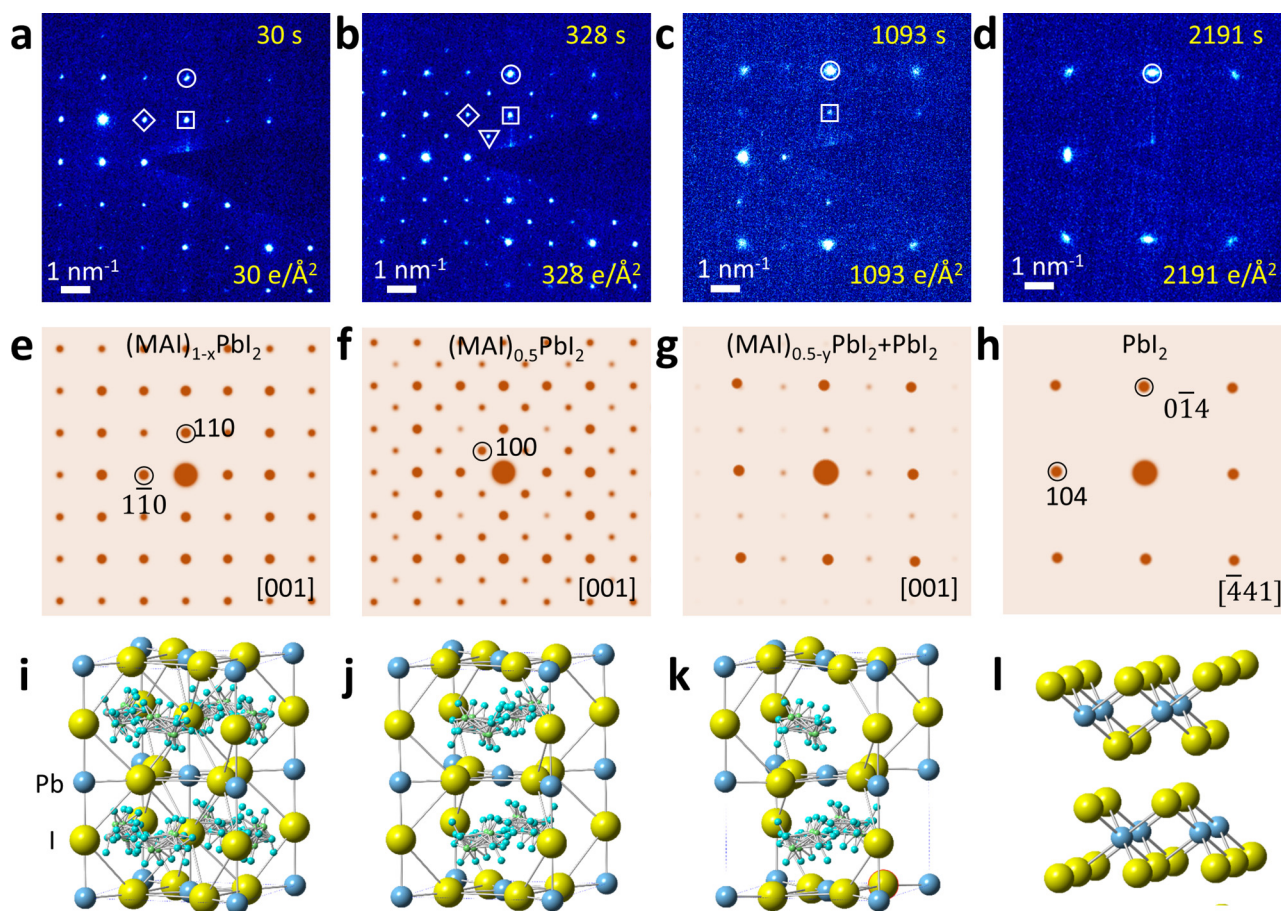
FIG. 4. The structural evolution during decomposition from MAPbI$_3$ to PbI$_2$. (a)–(d) Time-series SAED patterns showing the structure transformation under a dose rate of 1e Å^{-2} s^{-1}. The cumulative electron dose and time are labeled on each ED pattern. (e)–(h) The corresponding simulated ED patterns and (i)–(l) atomistic structures. These images are reproduced with permission from Chen *et al.*, Nat. Commun. **9**, 4807 (2018). Copyright 2018 Nature Publishing Group.

and ED patterns between MAPbI$_3$ and PbI$_2$, as shown in Fig. 5. PbI$_2$ has a variety of structures with different connections of Pb-I octahedron and the PbI$_2$ decomposed from MAPbI$_3$ is hexagonal[40] (Space group: R-3m:H, $a = b = 0.4557$ nm, $c = 2.0937$ nm, $\alpha = \beta = 90°$, and $\gamma = 120°$).[65] Figure 5(a) shows the atomistic structure and the corresponding simulated ED pattern along the [001] direction of MAPbI$_3$, which is easy to be mistaken as the ED pattern of PbI$_2$ along the [$\bar{4}$41] zone axis because of their extremely close reciprocal space distance [Fig. 5(b)]. Considering the critical dose for MAPbI$_3$–PbI$_2$ transition is as low as 2200 e Å^{-2} as shown in Fig. 4, the obtained ED patterns are usually PbI$_2$ rather than MAPbI$_3$ once the {110} reflections of MAPbI$_3$ are absent. Similarly, the ED patterns along the [10$\bar{1}$] and [021] directions of MAPbI$_3$ are also easy to be identified as the [8 10 1] and [$\bar{1}$11] direction of PbI$_2$, respectively, as shown in Figs. 5(c)–5(f). Despite the similar ED patterns, the corresponding atomistic structures are different, which helps to distinguish MAPbI$_3$ and PbI$_2$. In contrast, the mis-interpretation of ED patterns seems to rarely occur for

MAPbBr$_3$[66–71] likely due to its better stability.[72] Therefore, attention must be paid additionally while analyzing the electron microscopy data for these materials especially for MAPbI$_3$.

V. MINIMIZATION OF THE BEAM DAMAGE

It is important to investigate how to increase the critical damage-free doses during characterizations to extract the intrinsic information of the pristine samples. Recently, the electron beam sensitive lithium dendrites and the solid electrolyte interphase have been successfully characterized at an atomic scale by using the cryo-TEM,[73] which can freeze the native state of the specimen, capture reaction intermediates, and preserve volatile species.[28] Encouraged by the effectively decreasing beam damage under cryogenic condition, Li *et al.* established a cryo-EM protocol to reveal the atomic structure of MAPbI$_3$ as shown in Fig. 6.[74] The as-grown MAPbI$_3$ nanowires (NWs) were dropcast onto a Quantifoil TEM grid and then were plunge-frozen directly into the liquid nitrogen

TABLE I. Literature studies reporting on ED and FFT patterns of tetragonal MAPbI$_3$ from different directions.

| Zone axis	Absent reflections	Details or method	Reference
[001]	{110}	SAED and FFT	45
Unidentified	{110} {012}	FFT	46
[110]	{110} {002}	SAED and FFT	47
[-201]	{112}	FFT	48
[001]	{110}	SAED	49
[110]	{110} {002}	SAED and FFT	50
[110]	{110} {002}	SAED and FFT	51
[110]	{110} {002}	FFT	52
[001]	{110}	SAED	53
Unidentified	{101}	FFT	54
[001]	{110}	SAED	55
[201]	{112}	SAED	55
[001]	{110}	SAED	35
[001]	{110}	SAED	56
[001]	{110}	SAED	57
[001]	{110}	SAED and FFT	58
[001]	{110}	FFT	59
Unidentified	{110}	FFT	60
Unidentified	{110}	SAED	61
Unidentified	{101} {200}	SAED	62
[110]	{110} {002}	SAED	63
[001]	{110}	SAED	64

to prevent the side reactions, which can help retain the original state of the perovskite NWs at the cryogenic temperature, as shown in Fig. 6(a). Then, the specimen was transferred into the TEM column without exposure to the air and kept at −175 °C for TEM imaging, performed at 200 kV by using the direct-detection electron-counting (DDEC) camera. With the high detective quantum efficiency (DQE) of the DDEC camera, they have acquired the HRTEM images of MAPbI$_3$ and MAPbBr$_3$ NWs at doses of 12 e Å^{-2} and 46 e Å^{-2} [Fig. 6(b)], respectively. The higher dose for MAPbBr$_3$ suggests its better stability under the electron beam irradiation compared to that of MAPbI$_3$.[72] The structure evolution at −175 °C is further presented by the FFT patterns with the increased dose from 7.6 to 22.8 e Å^{-2}, as shown in Fig. 6(c). MAPbI$_3$ began to lose its crystallinity at the dose of 15.2 e Å^{-2} and showed severe structural damage at the dose of 22.8 e Å^{-2}. Despite that MAPbI$_3$ undergoes a tetragonal–orthorhombic transition at −108 °C,[75] Li et al. believed that such a structure change does not occur in their case likely due to the fast cooling of the plunge-freezing procedure. In a very recent cryo-TEM work by Zhu et al., the atomic steps of surface and stacking faults are observed in MAPbI$_3$ at 70–100 e Å^{-2},[76] as shown in Fig. 6(d). The FFT is consistent with the simulated ED along the [3$\bar{1}$0] direction, suggesting the successful acquisition of pristine MAPbI$_3$ structure. They further performed HRTEM simulations to interpret the observed structure and found the brightest atomic columns are identified to be MAI layers. Thus an MAI–MAI stacking fault along the (002) surface is observed by the red arrows, which alters the bandgap from 1.56 eV to 1.84 eV as verified by the density functional theory

(DFT) calculations. Such stalking faults are found to be stable under an exposure time of 32 s (1504 Å^{-2}) under electron beam irradiation at the cryogenic condition. However, in the work by Li et al.,[74] the FFT pattern at 7.6 e Å^{-2} already shows the superstructure spots as highlighted by the blue circles in Fig. 6(c), although it was not discussed in the paper. These additional reflections are either from the orthorhombic phase or caused by the ordered iodine vacancies, indicating that the damage has already occurred according to a previous study.[40] Whether or not the cryo-condition is beneficial to reduce the beam damage needs further evidence.

In another work, ED patterns have been used to study the effect of low temperature on beam damage by a liquid nitrogen side-entry specimen holder, as shown in Fig. 7. Rothmann et al.[42] cooled a single grain in polycrystal MAPbI$_3$ down to −180 °C and studied the structural evolution by ED under electron illumination, as shown in Fig. 7(a), wherein the pristine selected area electron diffraction (SAED) pattern is near the [21$\bar{6}$] direction of the orthorhombic MAPbI$_3$. It is observed that the sharp diffraction reflections continuously disappear and finally change into an amorphous ring within 1440 e Å^{-2}. In contrast, MAPbI$_3$ presents a crystal–crystal transition at room temperature (RT) within 3720 e Å^{-2}, despite the final product is not well recognized. Based on these observations, they proposed that the low temperature might not be helpful to reduce the beam damage. The atomic defects (interstitials and vacancies) generated by the electron irradiation are frozen at low temperature and become much less mobile;[30,77] thus, they are prone to be accumulated as clusters, further becoming amorphous. In another recent work,[78] Chen et al. also observed a similar fast crystal–amorphous transition at −180 °C within ~150 e Å^{-2} along the [001] direction of single-crystal MAPbI$_3$ as shown in Fig. 7(b), while it takes about 450 e Å^{-2} to induce the MAPbI$_3$–PbI$_2$ transition at RT. From the [100] direction, MAPbI$_3$ becomes amorphous within 129 e Å^{-2} at −180 °C [Fig. 7(c)], while it transforms into PbI$_2$ within 474 e Å^{-2} at RT. Such a crystal–amorphous transition at low temperature has also been observed in MAPbBr$_3$ and CsPbBr$_3$.[78,79] These data show that the dose for the crystal–amorphous transition at −180 °C is about 1/3 of that at RT to induce the MAPbI$_3$–PbI$_2$ transition, indicating the low temperature (−180 °C) does not slow down the beam damage but instead induces a rapid amorphization for OIHPs. As a result, the cryo-condition is not always suitable for TEM characterizations of OIHPs.

Besides the temperature, accelerating voltage is another important factor during the TEM characterizations. The low voltage is well known to be beneficial to decrease the knock-on damage, which has been widely used to image carbon nanotube and graphene.[80,81] However, a low voltage increases the radiolysis damage. It is reported that the decomposition of CsPbBr$_3$ is mainly due to the radiolysis damage; thus, a high accelerating voltage is helpful to reduce the damage.[82] So far, the successful examples of imaging OIHPs were mostly performed at a high voltage (200 or 300 kV), while the damage mechanism of OIHPs has not yet been investigated in detail. Thus, a recent work used the critical total dose (D_t) before the appearance of the superstructure spots as a reference to compare the beam sensitivity at 80 kV and 300 kV.[78] As shown in Fig. 8(a), D_t at 300 kV (38–39 e Å^{-2}) is about 2–3 times larger than that at 80 kV (13–16 e Å^{-2}). Thus, a lower voltage is expected to
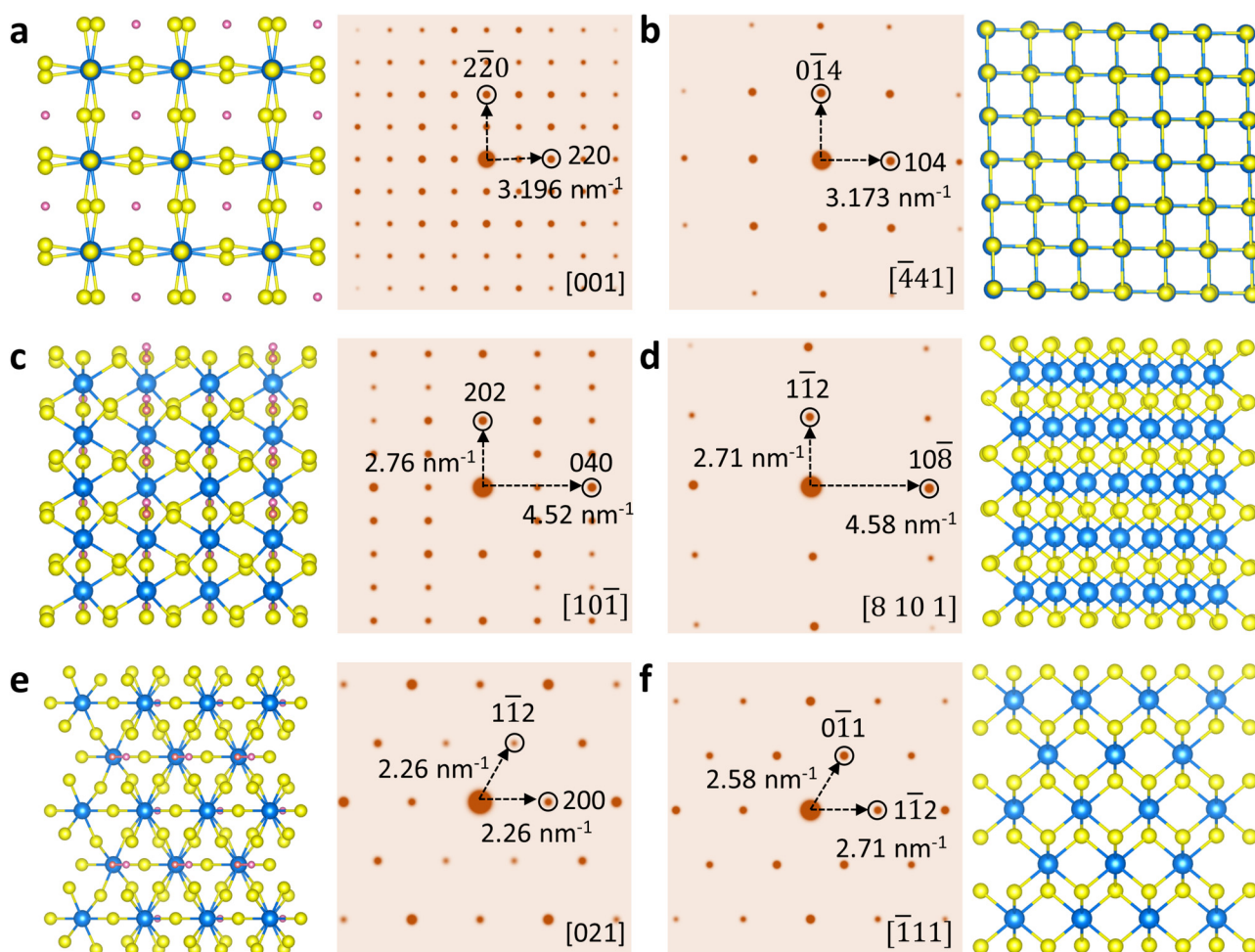
05 September 2023 02:30:25

FIG. 5. Differences in structure and ED pattern between MAPbI$_3$ and PbI$_2$. (a), (c), and (e) The atomistic structures and simulated ED patterns of MAPbI$_3$ along the [001], [10$\bar{1}$], and [021] directions, respectively. (b), (d), and (f) The atomistic structures and simulated ED patterns of PbI$_2$ along the [$\bar{4}$41], [8 10 1], and [$\bar{1}$11] directions, respectively.

cause severe beam damage, suggesting that knock-on damage is not the primary damage mechanism for OIHPs. Moreover, lowering temperature should help to reduce the heating damage, but instead, a rapid crystal–amorphous transition is observed at low temperature. Accordingly, the predominant damage mechanism for MAPbI$_3$ is radiolysis, which is consistent with its semi-conductor nature.[83] The identified electron beam damage mechanism can guide the future TEM characterizations of OIHPs that should be performed at a high voltage. Note that increasing the acceleration voltage higher will not only decrease the cross section of radiolysis but also increase the cross section of knock-on damage of OIHPs, leading to a change in the dominant damage mechanism;[84] whether or not ultrahigh voltage (e.g., MeV) is more suitable to characterize OIHPs needs further investigations.

Moreover, it is reported that the stability of MAPbI$_3$ is related with the exposure surface.[85] Lv *et al.* observed that (001) facet

exhibited higher sensitivity and faster erosion rate to water than the (100) face.[85] Chen *et al.* found that D_t for a (100) exposed plane ranges from 210 to 500 e Å^{-2}, which is about ten times larger than a (001) exposed plane (30–41 e Å^{-2}) for MAPbI$_3$, as shown in Fig. 8(b),[78] suggesting a facet-dependent electron beam sensitivity. This is likely due to an easier diffusion of iodine on (001) surface (0.32 eV) compared to that on (100) surface (0.45 eV).[86] Besides the TEM characterization, this finding also indicates that proper facet engineering such as growing (100)-textured perovskite films might improve the stability and performance of perovskite solar cells (PSCs).

Since OIHPs are easy to degrade under electron beam irradiation, it is vitally important to suppress the degradation and stabilize the structure of OIHPs for enhanced stability of PSCs. Fan *et al.* revealed a layer-by-layer degradation pathway of MAPbI$_3$ by TEM observations and DFT simulations.[58] Thus, they believe it is
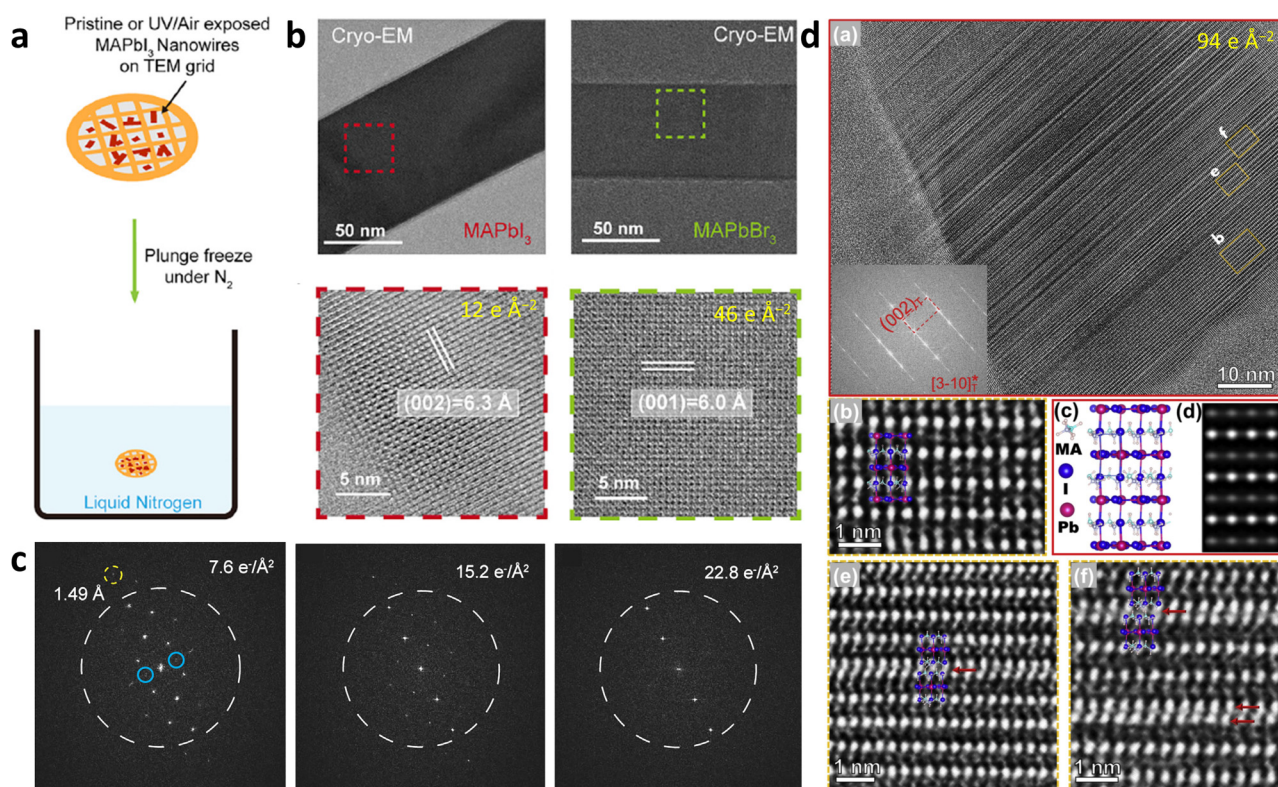
FIG. 6. Characterizations of MAPbI$_3$ by cryo-TEM. (a) Schematic illustration of the specimen preparation for cryo-TEM. (b) Low-magnification TEM and HRTEM images of MAPbI$_3$ and MAPbBr$_3$ under cryogenic conditions obtained at 200 kV with a dose of 12 Å^{-2} and 46 Å^{-2}, respectively. (c) *In situ* FFT patterns to show the structure evolution of MAPbI$_3$ with increased dose. The blue circles highlight the additional superstructure spots at 7.6 Å^{-2}. These images are reproduced with permission from Li *et al.*, Joule **3**, 2854–2866 (2019). Copyright 2019 Elsevier. (d) MAI–MAI type stacking faults observed in tetragonal MAPbI$_3$ along the [310] direction at a dose rate of ~47 Å^{-2} s^{-1} for 2 s. Reproduced with permission from Zhu *et al.*, Nano Energy **73**, 104820 (2020). Copyright 2019 Elsevier.

possible to slow down the layer-by-layer degradation by suppressing the structure transition on the surface layer. To verify this, they used hexagonal boron nitride (hBN) thin flakes as the encapsulation layer on the top and bottom surface of MAPbI$_3$ to fabricate the BN–MAPbI$_3$–BN heterostructure, as shown in Fig. 9(a). *In situ* SAED patterns show no distinguished structure changes after 30 min at 85 °C [Fig. 9(b)], while the non-encapsulated MAPbI$_3$ begins to decompose within 1 min and totally transforms into trigonal PbI$_2$ within 7 min, which suggests a much enhanced thermal stability of MAPbI$_3$ because of the hBN encapsulation. Further DFT calculations show that the degradation barrier increases by 0.05 eV for hBN encapsulated MAPbI$_3$ surface than that of the unencapsulated surface. Although the experimental design and conclusions seem rational, the authors ignored the effect of the electron beam irradiation and in fact the SAED pattern at 0 s before heating is hexagonal PbI$_2$ along the [$\bar{4}$41] direction rather than the [110] direction of MAPbI$_3$ as discussed in Fig. 5. Thus, whether or not the hBN encapsulation can improve the thermal stability still requires more experimental evidence.

Besides hBN, other surface coating materials on both sides of the TEM specimen are also effective to decrease the mass loss and

suppress the loss of the crystallinity.[29] The thin carbon layers were coated on both sides of MAPbI$_3$ with a thickness of about 6–10 nm as shown in Fig. 9(c).[44] Under electron beam illumination, the uncoated MAPbI$_3$ decomposes into PbI$_2$ within 791 Å^{-2} with the disappearance of the characteristic (002)$_C$ spot. The HAADF-STEM image of PbI$_2$ is shown in Fig. 9(d). In contrast, the (002)$_C$ reflection of the coated MAPbI$_3$ maintains at 7600 Å^{-2} [Fig. 9(f)]. The (002)$_C$ intensity changes vs time for coated and uncoated specimen are shown in Fig. 9(e), suggesting that the carbon coating can stabilize the MAPbI$_3$ structure framework and thus suppress the degradation of MAPbI$_3$. The enhanced stability is because the coating layer can serve as a diffusion barrier, reducing the escape rate of the volatile species,[29,32] as proved by the EDS results. Such a coating method is easy to achieve and effective to stabilize the structure, which might be useful to design more stable PSCs.

VI. ATOMIC IMAGING OF THE STRUCTURE

Although the ED pattern of pristine OIHPs is feasible once the electron dose is carefully controlled, the atomic imaging of
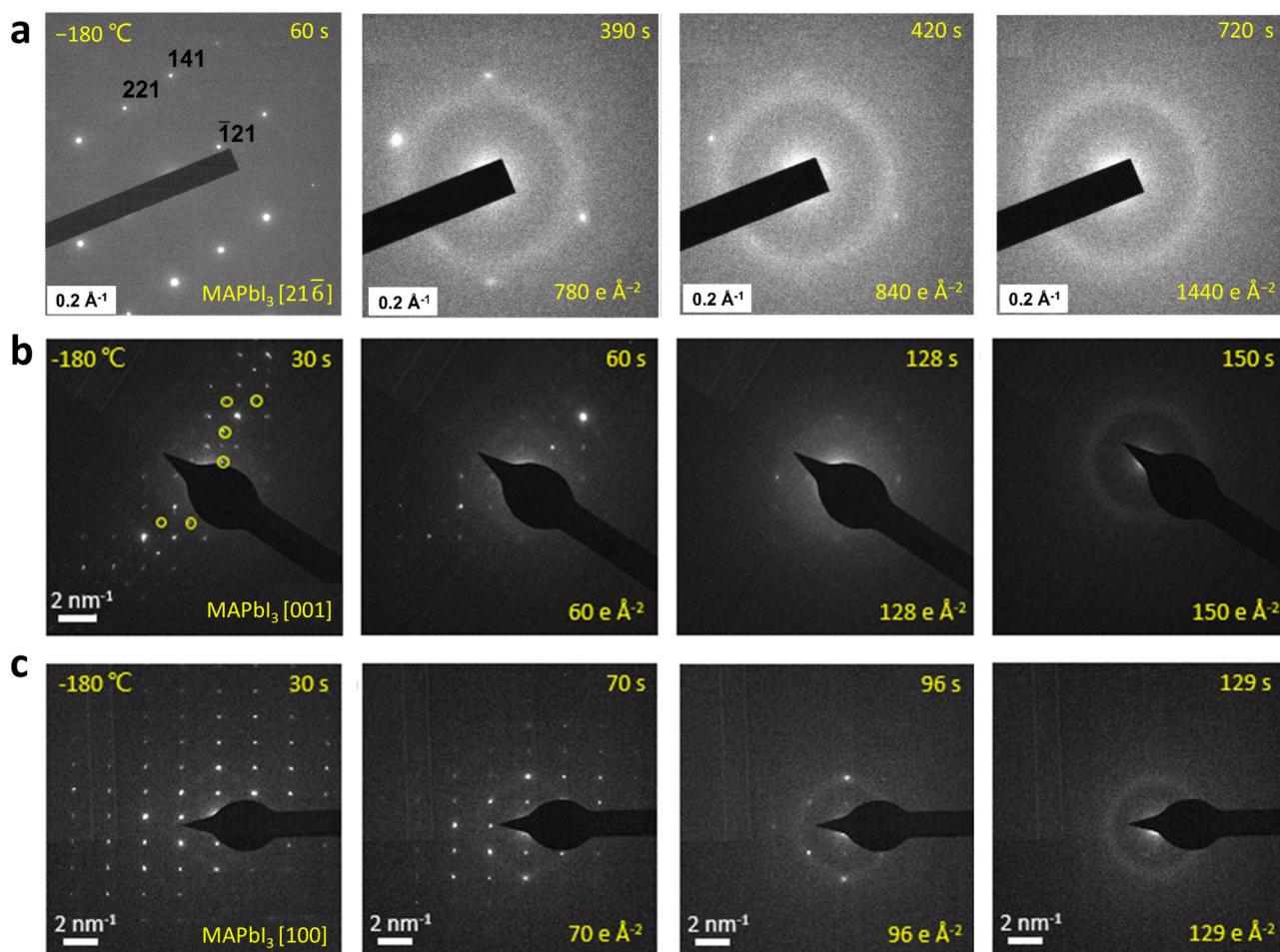
FIG. 7. The effect of cooling on the structure evolution of MAPbI₃. (a)–(c) Time-series SAED patterns of MAPbI₃ at −180 °C along the [21̄6̄], [001], and [100] directions, respectively. The image in (a) is reproduced with permission from Rothmann *et al.*, Adv. Mater. **30**, 1800629 (2018). Copyright 2018 Wiley-VCH. The images in (b) and (c) are reproduced with permission from Chen *et al.*, "Transmission electron microscopy of organic-inorganic hybrid perovskites: myths and truths," Sci. Bull. (2020). Copyright 2020 Elsevier.
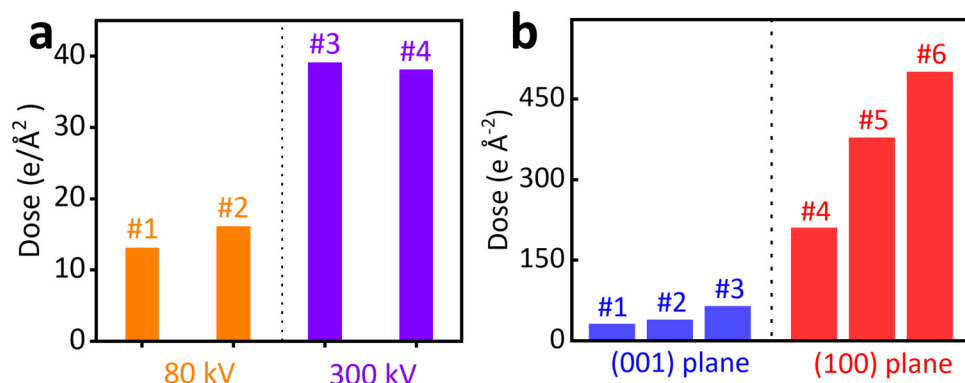

FIG. 8. The effect of accelerating voltage and exposed surface on the beam sensitivity. The total dose before generating superstructure spots (a) at 80 kV and 300 kV and (b) for (001) and (100) exposed surface. Reproduced with permission from Chen *et al.*, "Transmission electron microscopy of organic-inorganic hybrid perovskites: myths and truths," Sci. Bull. (2020). Copyright 2020 Elsevier.
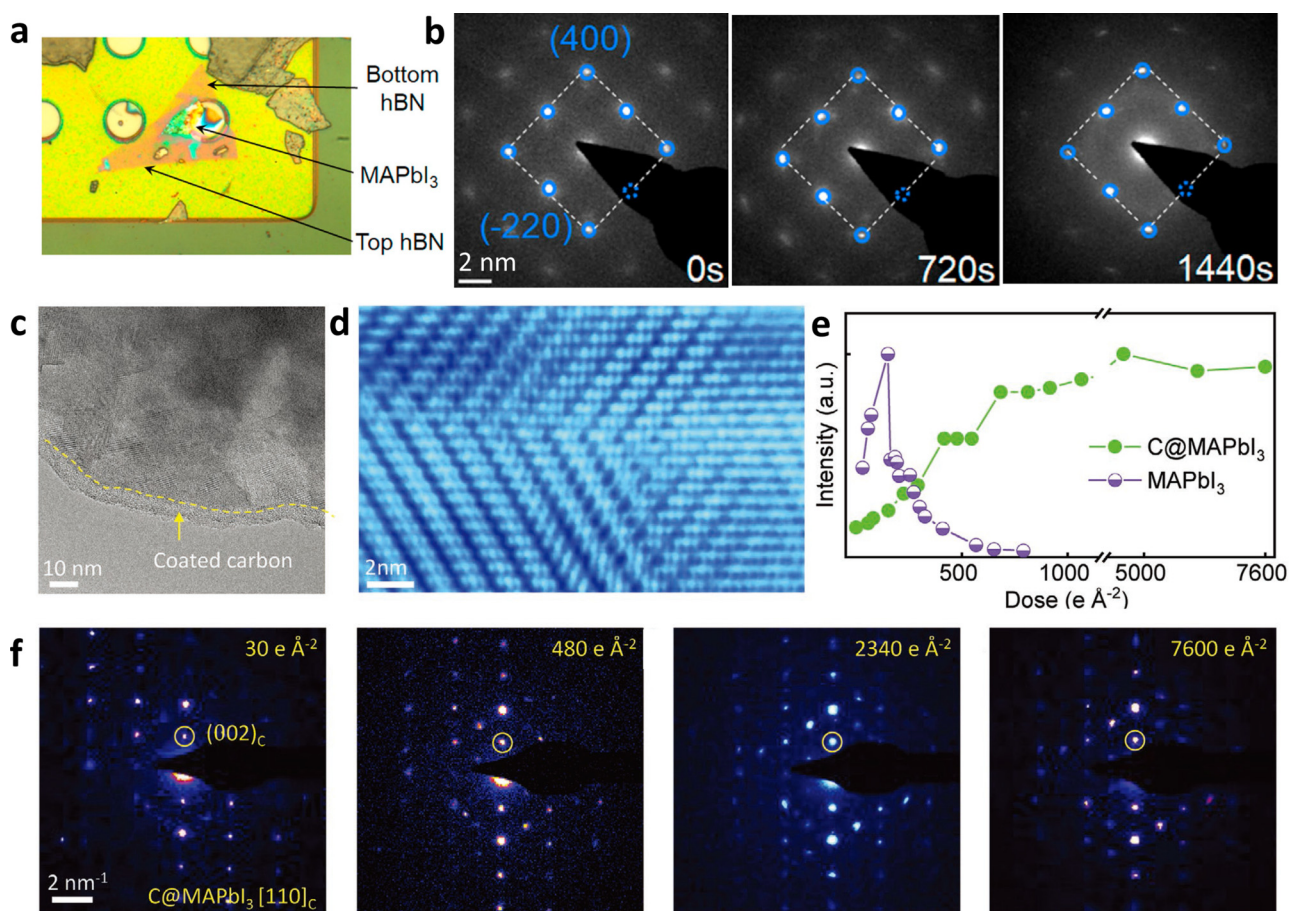
FIG. 9. Suppression of the degradation via coating. (a) The photography of BN–MAPbI$_3$–BN heterostructure. (b) *In situ* SAED patterns of the BN–MAPbI$_3$–BN heterostructure under continuous heating at 85 °C in vacuum. The images in (a) and (b) are reproduced with permission from Fan *et al.*, Joule **1**, 548–562 (2017). Copyright 2017 Elsevier. (c) HRTEM image with a 6–10 nm carbon layer coated on MAPbI$_3$. (d) HAADF-STEM image of PbI$_2$ along the [110] direction. (e) The intensities of (002)$_C$ reflection are plotted as a function of time. (f) Time-series SAED patterns along the [110]$_C$ direction of carbon-coated MAPbI$_3$ with total dose. The dose rate is 1 e Å^{-2} s^{-1} at 300 kV for SAED imaging. The images in (c)–(f) are reproduced with permission from Chen *et al.*, Adv. Mater. 2001107 (2020). Copyright 2020 Wiley-VCH.

OIHPs that typically requires much higher dose remains challenging.[40,42] To solve the problem, it requires strategies to capture the structure with a sufficient low electron dose before the damage occurs, via either increasing the critical dose with optimized imaging conditions mentioned above or using better data recording equipment to collect the signals at ultralow doses. One solution is to use the DDEC camera with a high DQE,[87,88] which has been widely used to improve the resolution for biological macromolecules.[89] However, to obtain the atomic structure of these beam sensitive crystalline materials by the DDEC camera, it requires a rapid on-axis adjustment for crystals to decrease the beam damage, precise alignment of the successive short-exposure images to avoid the loss of resolution, and accurate determination of the defocus to interpret the image.[28] To overcome these obstacles, Zhang *et al.* developed a simple program to achieve a direct alignment of the zone axis within 1 e Å^{-2} for a small deviation in the crystal

orientation ($-5° < \varphi < 5°$), an "amplitude filter" to extract the high-resolution information hidden in the image stack, and a method to determine the defocus value.[28] With these solutions, they successfully obtained the atomic-resolution HRTEM image of MAPbBr$_3$ at a dose of 11 e Å^{-2}. After correcting the "contrast inversion" caused by the contrast transfer function (CTF) of the objective lens, it is revealed that MAPbBr$_3$ crystals contain ordered nanodomains with off-centered MA cations showing normal and parallel configurations [Fig. 10(a)], which suggests the possible ferroelectric order in this material or specimen mistilt/residual coma.[90] With the similar method, the HRTEM image of MAPbI$_3$ [Fig. 10(b)] was also obtained recently at a dose of 3.1 e Å^{-2} wherein the corresponding FFT [Fig. 10(c)] is consistent with the simulated ED pattern of tetragonal MAPbI$_3$ without any superstructure reflections. Besides the HRTEM imaging, Song *et al.*[91] acquired the STEM image of MAPbBr$_3$ at a dose of 280 e Å^{-2} as shown in Figs. 10(d) and 10(e)
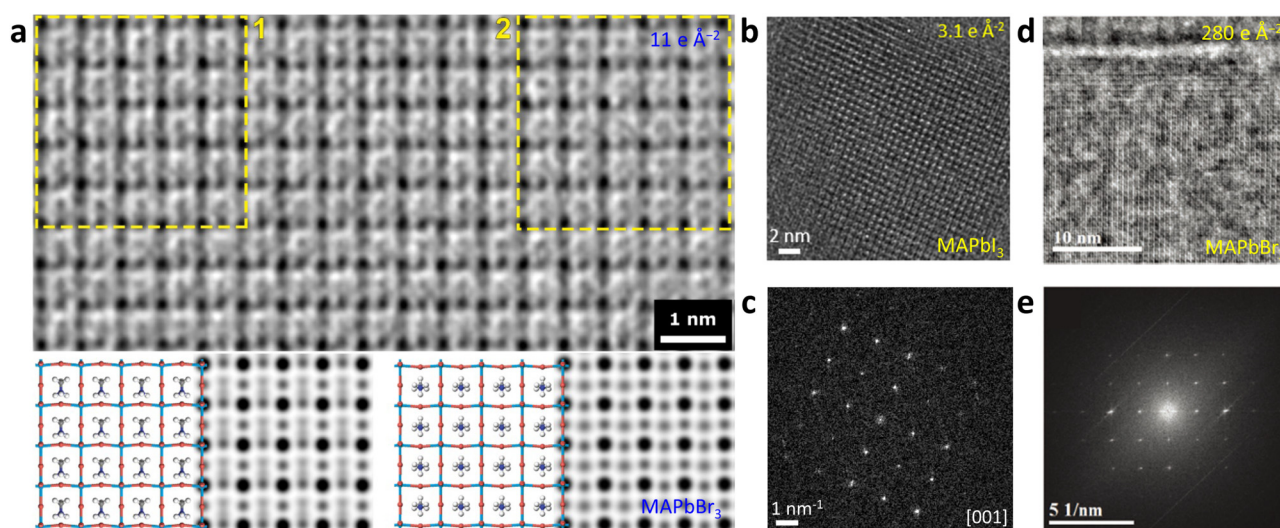
FIG. 10. Atomic imaging of OIHPs. (a) CTF-corrected HRTEM image of MAPbBr$_3$. Regions 1 and 2 show two nanodomains with different orientations of MA cation. Reproduced with permission from Zhang *et al.*, Science, **359**, 675–679 (2018). Copyright 2018 American Association for the Advancement of Science. (b) HRTEM image and (c) the corresponding FFT pattern along the [001] direction of MAPbI$_3$ acquired at 3.1 e Å^{-2} at 300 kV. Reproduced with permission from Chen *et al.*, "Transmission electron microscopy of organic-inorganic hybrid perovskites: myths and truths," Sci. Bull. (2020). Copyright 2020 Elsevier. (d) iDPC-STEM image and (e) the corresponding FFT pattern of MAPbBr$_3$ (pixel size: 0.51 Å; beam current: 2 pA; dwell time: 6 μs; and total dose: 280 e Å^{-2}). Reproduced with permission from Song *et al.*, Adv. Energy Mater. 1904006 (2020). Copyright 2020 Wiley-VCH.

by using the low-dose integrated differential phase contrast (iDPC)-STEM imaging technique,[92] which again suggests that MAPbBr$_3$ has better stability.

VII. SUMMARY AND OUTLOOK

In this perspective, we mainly discuss how the electron beam destabilizes the OIHPs during characterizations and what are the degradation pathway and the optimal TEM operation conditions. We are intending to catch researchers' attention on electron beam sensitivity, guide the TEM characterization, and inspire the development to reveal the real degradation mechanism of the OIHPs and the practical failure mechanism of OIHP-based solar cells.

In a large number of studies, TEM characterizations were performed at a large dose with the beam sensitivity being ignored. Therefore, there are inconsistencies between the expected and experimental data of MAPbI$_3$ even for the ED patterns that require relatively low doses. Considering the dose rates under HRTEM, STEM, EELS, and EDS are comparably higher than that of ED, severe damage is expected. The positive side of the damage helps us understand the failure mechanism of these materials and the devices based on them. Considering that the energy transfer is essential for the electron-beam-induced damage, which is similar to that caused by heating, light illumination, and electrical bias, the discovered degradation pathway in the electron microscope delivers some useful insights into understanding the failure mechanism in practical devices. Indeed, it has been reported that the degradation pathway observed under electron beam illumination, i.e., MAPbI$_3$ degrades into PbI$_2$ with the removal of MAI,[40] is in good

agreement with the decomposition processes observed under light illumination,[16] heating,[93] and DFT calculations[94] but with much better spatial resolution and greater structural details. On the other hand, the suppression strategy for the degradation of OIHPs such as coating[44,58] and the corresponding working mechanism can also be mimicked in the microscope. It should be noted that although there are some *in situ* TEM studies on the failure mechanism of OIHPs and devices based on them, the electron beam induced damage likely makes some contributions to the observed phenomena considering the large electron doses they used.

Therefore, to avoid misinterpretation of experimental data, great attention should be paid during the characterizations to keep the dose low not only for *in situ* TEM but also for regular electron microscopy characterizations. High voltage, coating, thin sample, and proper zone axis should be helpful to mitigate the damage due to the radiolysis nature, while for the cryo-TEM method, the validity is still under debate. The inconsistencies between previous literature studies[42,74,76,78] may be due to the difference between the cryo-holder and cryo-microscope methods, or the discrepancy of specimens in different studies. Actually, the specimens prepared by cryo-EM method are naturally coated with an amorphous ice layer,[95] which may serve as a protective layer to slow down the beam damage, while the general cryo-holder can only produce low-temperature without any coating layer. Nevertheless, further controlled studies are needed to clarify if low-temperature or coating dominates the cryoprotection for OIHPs.

Besides, the data recording system is also vital to reduce the damage. Atomically resolved images of MAPbBr$_3$ were successfully acquired by iDPC-STEM, and the HRTEM images of MAPbI$_3$ were

captured by the DDEC cameras, suggesting that atomic imaging of these materials is certainly feasible. We can expect other low-dose imaging techniques or recording systems such as electron ptychography and 4D-STEM will also be employed to study these materials in near future to explore not only the structure but also the potential and charge information.

In any case, as a rough estimation, the electron dose should be below $\sim 100\,\mathrm{e\,Å^{-2}}$ for MAPbI$_3$; otherwise, substantial damage occurs during TEM characterizations. The ED data are generally reliable for MAPbBr$_3$ and inorganic CsPbBr$_3$ is typically safe even for regular STEM and spectroscopy characterizations.

The reliable and robust imaging would enable more extensive investigations on the structure–property relationships for these materials. For example, previous piezoresponse force microscopy characterizations show the striped domain structures in MAPbI$_3$,[96] and whether they are polar or non-polar are still under intensive debate.[97] In fact, Zhang *et al.* have made great progress based on the HRTEM image of MAPbBr$_3$; they propose possible ferroelectric order in this material,[28] although more careful and quantitative studies are needed to verify this conclusion because the atomic displacement in the image is also sensitive to the specimen mistilt/residual coma,[90] which can cause significant artifact and misinterpretation for experimental data. Nevertheless, ultimately, the atomically resolved electron microscopy imaging and convergent beam electron diffraction would answer these polar and non-polar questions once the damage issue is overcome. Besides, the atomic structure of defects such as point defects,[98] stacking faults,[76] and domain walls[41] can be determined, and their roles on the optoelectronic and electromechanical properties[98,99] can be revealed by the atomic arrangements combined with the theoretical analysis based on the atomic-resolution images. Furthermore, many *in situ* TEM studies on not only the thermal stability[100,101] and degradation process[79,82] but also the working principles under optical illumination[102] and possible ferroelectric domain switching[103,104] can be performed with the microscopes.

DATA AVAILABILITY

The data that support the findings of this study are available from the corresponding author upon reasonable request.

REFERENCES

[1]N. Li, S. Tao, Y. Chen, X. Niu, C. K. Onwudinanti, C. Hu, Z. Qiu, Z. Xu, G. Zheng, and L. Wang, Nat. Energy 4, 408 (2019).
[2]X. Li, D. Bi, C. Yi, J. Décoppet, J. Luo, S. M. Zakeeruddin, A. Hagfeldt, and M. Grätzel, Science 353, 58 (2016).
[3]P. Liu, X. He, J. Ren, Q. Liao, J. Yao, and H. Fu, ACS Nano 11, 5766–5773 (2017).
[4]S. A. Veldhuis, P. P. Boix, N. Yantara, M. Li, T. C. Sum, N. Mathews, and S. G. Mhaisalkar, Adv. Mater. 28, 6804–6834 (2016).
[5]N. Wang, L. Cheng, R. Ge, S. Zhang, Y. Miao, W. Zou, C. Yi, Y. Sun, Y. Cao, and R. Yang, Nat. Photonics 10, 699–704 (2016).
[6]H. Cho, S. Jeong, M. Park, Y. Kim, C. Wolf, C. Lee, J. H. Heo, A. Sadhanala, N. Myoung, and S. Yoo, Science 350, 1222–1225 (2015).
[7]A. Kojima, K. Teshima, Y. Shirai, and T. Miyasaka, J. Am. Chem. Soc. 131, 6050–6051 (2009).
[8]National Renewable Energy Laboratory (NREL), Efficiency records chart, see https://www.nrel.gov/pv/cell-efficiency.html; accessed June 2020.
[9]D. Bryant, N. Aristidou, S. Pont, I. Sanchez-Molina, T. Chotchunangatchaval, S. Wheeler, J. R. Durrant, and S. A. Haque, Energy Environ. Sci. 9, 1655–1660 (2016).
[10]R. Xia, Z. Fei, N. Drigo, F. D. Bobbink, Z. Huang, R. Jasiūnas, M. Franckevičius, V. Gulbinas, M. Mensi, and X. Fang, Adv. Funct. Mater. 29, 1902021 (2019).
[11]W. Huang, S. Sadhu, and S. Ptasinska, Chem. Mater. 29, 8478–8485 (2017).
[12]N. Kim, Y. H. Min, S. Noh, E. Cho, G. Jeong, M. Joo, S. Ahn, J. S. Lee, S. Kim, K. Ihm, H. Ahn, Y. Kang, H. Lee, and D. Kim, Sci. Rep. UK 7, 4645 (2017).
[13]J. Yang, B. D. Siempelkamp, D. Liu, and T. L. Kelly, ACS Nano 9, 1955–1963 (2015).
[14]Q. Jeangros, M. Duchamp, J. Werner, M. Kruth, R. E. Dunin-Borkowski, B. Niesen, C. Ballif, and A. Hessler-Wyser, Nano Lett. 16, 7013–7018 (2016).
[15]Y. Yuan, Q. Wang, Y. Shao, H. Lu, T. Li, A. Gruverman, and J. Huang, Adv. Energy Mater. 6, 1501803 (2016).
[16]R. Xu, Y. Li, T. Jin, Y. Liu, Q. Bao, C. O. Carroll, and J. Tang, ACS Appl. Mater. Interfaces 10, 6737–6746 (2018).
[17]G. Abdelmageed, L. Jewell, K. Hellier, L. Seymour, B. Luo, F. Bridges, J. Z. Zhang, and S. Carter, Appl. Phys. Lett. 109, 233905 (2016).
[18]A. R. Milosavljević, W. Huang, S. Sadhu, and S. Ptasinska, Angew. Chem. Int. Ed. 55, 10083–10087 (2016).
[19]N. Klein-Kedem, D. Cahen, and G. Hodes, Acc. Chem. Res. 49, 347–354 (2016).
[20]H. Yuan, E. Debroye, K. Janssen, H. Naiki, C. Steuwe, G. Lu, M. Moris, E. Orgiu, H. Uji-i, F. De Schryver, P. Samorì, J. Hofkens, and M. Roeffaers, J. Phys. Chem. Lett. 7, 561–566 (2016).
[21]S. Ito, S. Tanaka, K. Manabe, and H. Nishino, J. Phys. Chem. C 118, 16995–17000 (2014).
[22]C. Li, S. Tscheuschner, F. Paulus, P. E. Hopkinson, J. Kießling, A. Köhler, Y. Vaynzof, and S. Huettner, Adv. Mater. 28, 2446–2454 (2016).
[23]Y. Yuan and J. Huang, Acc. Chem. Res. 49, 286–293 (2016).
[24]F. U. Kosasih and C. Ducati, Nano Energy 47, 243–256 (2018).
[25]M. Telychko and J. Lu, Nano Mater. Sci. 1, 260–267 (2019).
[26]E. M. Tennyson, T. A. S. Doherty, and S. D. Stranks, Nat. Rev. Mater. 4, 573–587 (2019).
[27]D. B. Williams and C. B. Carter, *Transmission Electron Microscopy: A Textbook for Materials Science*, 2nd ed. (Springer, New York, 2009).
[28]D. Zhang, Y. Zhu, L. Liu, X. Ying, C. Hsiung, R. Sougrat, K. Li, and Y. Han, Science 359, 675–679 (2018).
[29]R. F. Egerton, P. Li, and M. Malac, Micron 35, 399–409 (2004).
[30]R. F. Egerton, Micron 119, 72–87 (2019).
[31]L. W. Hobbs, *Quantitative Electron Microscopy* (Plenum Press, New York, 1984).
[32]R. F. Egerton, P. A. Crozier, and P. Rice, Ultramicroscopy 23, 305–312 (1987).
[33]X. Chen and Z. Wang, Micron 116, 73–79 (2019).
[34]A. Alberti, C. Bongiorno, E. Smecca, I. Deretzis, A. La Magna, and C. Spinella, Nat. Commun. 10, 2196 (2019).
[35]D. Li, G. Wang, H. Cheng, C. Chen, H. Wu, Y. Liu, Y. Huang, and X. Duan, Nat. Commun. 7, 11330 (2016).
[36]L. Niu, X. Liu, C. Cong, C. Wu, D. Wu, T. R. Chang, H. Wang, Q. Zeng, J. Zhou, X. Wang, W. Fu, P. Yu, Q. Fu, S. Najmaei, Z. Zhang, B. I. Yakobson, B. K. Tay, W. Zhou, H. T. Jeng, H. Lin, T. C. Sum, C. Jin, H. He, T. Yu, and Z. Liu, Adv. Mater. 27, 7800–7808 (2015).

05 September 2023 02:30:25

[37]B. Yang, O. Dyck, W. Ming, M. H. Du, S. Das, C. M. Rouleau, G. Duscher, D. B. Geohegan, and K. Xiao, ACS Appl. Mater. Interfaces 8, 32333–32340 (2016).

[38]G. Divitini, S. Cacovich, F. Matteocci, L. Cinà, A. Di Carlo, and C. Ducati, Nat. Energy 1, 15012 (2016).

[39]T. W. Kim, N. Shibayama, L. Cojocaru, S. Uchida, T. Kondo, and H. Segawa, Adv. Funct. Mater. 28, 1804039 (2018).

[40]S. Chen, X. Zhang, J. Zhao, Y. Zhang, G. Kong, Q. Li, N. Li, Y. Yu, N. Xu, J. Zhang, K. Liu, Q. Zhao, J. Cao, J. Feng, X. Li, J. Qi, D. Yu, J. Li, and P. Gao, Nat. Commun. 9, 4807 (2018).

[41]M. U. Rothmann, W. Li, Y. Zhu, U. Bach, L. Spiccia, J. Etheridge, and Y. Cheng, Nat. Commun. 8, 14547 (2017).

[42]M. U. Rothmann, W. Li, Y. Zhu, A. Liu, Z. Ku, U. Bach, J. Etheridge, and Y. Cheng, Adv. Mater. 30, 1800629 (2018).

[43]D. I. Woodward and I. M. Reaney, Acta Crystallogr. Sect. B Struct. Sci. 61, 387–399 (2005).

[44]S. Chen, Y. Zhang, X. Zhang, J. Zhao, Z. Zhao, X. Su, Z. Hua, J. Zhang, J. Cao, J. Feng, X. Wang, X. Li, J. Qi, J. Li, and P. Gao, Adv. Mater., 2001107 (2020).

[45]M. Xiao, F. Huang, W. Huang, Y. Dkhissi, Y. Zhu, J. Etheridge, A. Gray-Weale, U. Bach, Y. Cheng, and L. Spiccia, Angew. Chem. Int. Ed. 53, 9898–9903 (2014).

[46]C. A. H. L. Zhenhua, Mater. Res. Express 1, 015034 (2014).

[47]H. Zhu, Y. Fu, F. Meng, X. Wu, Z. Gong, Q. Ding, M. V. Gustafsson, M. T. Trinh, S. Jin, and X. Zhu, Nat. Mater. 14, 636–642 (2015).

[48]Z. Ning, X. Gong, R. Comin, G. Walters, F. Fan, O. Voznyy, E. Yassitepe, A. Buin, S. Hoogland, and E. H. Sargent, Nature 523, 324–328 (2015).

[49]M. Yang, Y. Zhou, Y. Zeng, C. Jiang, N. P. Padture, and K. Zhu, Adv. Mater. 27, 6363–6370 (2015).

[50]T. Kollek, D. Gruber, J. Gehring, E. Zimmermann, L. Schmidt-Mende, and S. Polarz, Angew. Chem. Int. Ed. 54, 1341–1346 (2015).

[51]B. Yang, O. Dyck, J. Poplawsky, J. Keum, S. Das, A. Puretzky, T. Aytug, P. C. Joshi, C. M. Rouleau, G. Duscher, D. B. Geohegan, and K. Xiao, Angew. Chem. Int. Ed. 54, 14862–14865 (2015).

[52]F. Zhu, L. Men, Y. Guo, Q. Zhu, U. Bhattacharjee, P. M. Goodwin, J. W. Petrich, E. A. Smith, and J. Vela, ACS Nano 9, 2948–2959 (2015).

[53]Y. Zhou, A. L. Vasiliev, W. Wu, M. Yang, S. Pang, K. Zhu, and N. P. Padture, J. Phys. Chem. Lett. 6, 2292–2297 (2015).

[54]A. Alberti, I. Deretzis, G. Pellegrino, C. Bongiorno, E. Smecca, G. Mannino, F. Giannazzo, G. G. Condorelli, N. Sakai, T. Miyasaka, C. Spinella, and A. La Magna, ChemPhysChem 16, 3064–3071 (2015).

[55]D. Son, J. Lee, Y. J. Choi, I. Jang, S. Lee, P. J. Yoo, H. Shin, N. Ahn, M. Choi, D. Kim, and N. Park, Nat. Energy 1, 16081 (2016).

[56]L. Gao, K. Zeng, J. Guo, C. Ge, J. Du, Y. Zhao, C. Chen, H. Deng, Y. He, H. Song, G. Niu, and J. Tang, Nano Lett. 16, 7446–7454 (2016).

[57]C. Zhao, W. Tian, J. Leng, R. Cui, W. Liu, and S. Jin, Sci. Bull. 61, 665–669 (2016).

[58]Z. Fan, Z. Xiao, Y. Wang, Z. Zhao, Z. Lin, H. Cheng, S. Lee, G. Wang, Z. Feng, W. A. Goddard, Y. Huang, and X. Duan, Joule 1, 548–562 (2017).

[59]M. Long, T. Zhang, H. Zhu, G. Li, F. Wang, W. Guo, Y. Chai, W. Chen, Q. Li, K. S. Wong, J. Xu, and K. Yan, Nano Energy 33, 485–496 (2017).

[60]S. Kim, S. Bae, S. Lee, K. Cho, K. D. Lee, H. Kim, S. Park, G. Kwon, S. Ahn, H. Lee, Y. Kang, H. Lee, and D. Kim, Sci. Rep. 7, 1200 (2017).

[61]J. Su, D. Lu, L. Zhang, D. Wang, Y. Bai, and W. Wang, Cryst. Res. Technol. 52, 1700171 (2017).

[62]M. Chen, J. Yang, Z. Wang, Z. Xu, H. Lee, H. Lee, Z. Zhou, S. P. Feng, S. Lee, J. Pyo, S. K. Seol, D. K. Ki, and J. T. Kim, Adv. Mater. 31, 1904073 (2019).

[63]G. Tang, P. You, Q. Tai, A. Yang, J. Cao, F. Zheng, Z. Zhou, J. Zhao, P. K. L. Chan, and F. Yan, Adv. Mater. 31, 1807689 (2019).

[64]S. Li, Y. Li, Z. Shi, L. Lei, H. Ji, D. Wu, T. Xu, X. Li, and G. Du, Sol. Energy Mat. Sol. Cells 191, 275–282 (2019).

[65]R. W. Wyckoff, Crystal Structure, 2nd ed. (Interscience Publishers Press, New York, 1993), Vol. 1, pp. 239–444.

[66]Q. Van Le, H. W. Jang, and S. Y. Kim, Small Methods 2, 1700419 (2018).

[67]H. Gao, J. Feng, Y. Pi, Z. Zhou, B. Zhang, Y. Wu, X. Wang, X. Jiang, and L. Jiang, Adv. Funct. Mater. 28, 1804349 (2018).

[68]H. Zhang, Q. Liao, X. Wang, J. Yao, and H. Fu, Adv. Opt. Mater. 4, 1718–1725 (2016).

[69]W. Zhang, L. Peng, J. Liu, A. Tang, J. Hu, J. Yao, and Y. S. Zhao, Adv. Mater. 28, 4040–4046 (2016).

[70]A. B. Wong, M. Lai, S. W. Eaton, Y. Yu, E. Lin, L. Dou, A. Fu, and P. Yang, Nano Lett. 15, 5519–5524 (2015).

[71]J. Wang, S. P. Senanayak, J. Liu, Y. Hu, Y. Shi, Z. Li, C. Zhang, B. Yang, L. Jiang, D. Di, A. V. Ievlev, O. S. Ovchinnikova, T. Ding, H. Deng, L. Tang, Y. Guo, J. Wang, K. Xiao, D. Venkateshvaran, L. Jiang, D. Zhu, and H. Sirringhaus, Adv. Mater. 31, 1902618 (2019).

[72]M. Shahbazi and H. Wang, Sol. Energy 123, 74–87 (2016).

[73]Y. Li, Y. Li, A. Pei, K. Yan, Y. Sun, C. L. Wu, L. M. Joubert, R. Chin, A. L. Koh, Y. Yu, J. Perrino, B. Butz, S. Chu, and Y. Cui, Science 358, 506–510 (2017).

[74]Y. Li, W. Zhou, Y. Li, W. Huang, Z. Zhang, G. Chen, H. Wang, G. Wu, N. Rolston, R. Vila, W. Chiu, and Y. Cui, Joule 3, 2854–2866 (2019).

[75]P. S. Whitfield, N. Herron, W. E. Guise, K. Page, Y. Q. Cheng, I. Milas, and M. K. Crawford, Sci. Rep. 6, 35685 (2016).

[76]Y. Zhu, Z. Gui, Q. Wang, F. Meng, S. Feng, B. Han, P. Wang, L. Huang, H. Wang, and M. Gu, Nano Energy 73, 104820 (2020).

[77]D. Yang, W. Ming, H. Shi, L. Zhang, and M. Du, Chem. Mater. 28, 4349–4357 (2016).

[78]S. Chen, Y. Zhang, J. Zhao, Z. Mi, J. Zhang, J. Cao, J. Feng, G. Zhang, J. Qi, J. Li, and P. Gao, "Transmission electron microscopy of organic-inorganic hybrid perovskites: myths and truths," Sci. Bull. (in press) (2020).

[79]Z. Dang, J. Shamsi, Q. A. Akkerman, M. Imran, G. Bertoni, R. Brescia, and L. Manna, ACS Omega 2, 5660–5665 (2017).

[80]M. Kühne, F. Börrnert, S. Fecher, M. Ghorbani-Asl, J. Biskupek, D. Samuelis, A. V. Krasheninnikov, U. Kaiser, and J. H. Smet, Nature 564, 234–239 (2018).

[81]A. Hashimoto, K. Suenaga, A. Gloter, K. Urita, and S. Iijima, Nature 430, 870–873 (2004).

[82]Z. Dang, J. Shamsi, F. Palazon, M. Imran, Q. A. Akkerman, S. Park, G. Bertoni, M. Prato, R. Brescia, and L. Manna, ACS Nano 11, 2124–2132 (2017).

[83]R. F. Egerton, Ultramicroscopy 127, 100–108 (2013).

[84]R. Csencsits and R. Gronsky, Ultramicroscopy 23, 421–431 (1987).

[85]Q. Lv, H. He, W. Z. Lian, Z. Ding, Q. Li, and Q. Yan, CrystEngComm 19, 901–904 (2017).

[86]J. Haruyama, K. Sodeyama, L. Han, and Y. Tateyama, J. Am. Chem. Soc. 137, 10048–10051 (2015).

[87]X. Li, P. Mooney, S. Zheng, C. R. Booth, M. B. Braunfeld, S. Gubbens, D. A. Agard, and Y. Cheng, Nat. Methods 10, 584–590 (2013).

[88]G. McMullan, S. Chen, R. Henderson, and A. R. Faruqi, Ultramicroscopy 109, 1126–1143 (2009).

[89]R. Fernandez-Leiro and S. H. W. Scheres, Nature 537, 339–346 (2016).

[90]P. Gao, A. Kumamoto, R. Ishikawa, N. Lugg, N. Shibata, and Y. Ikuhara, Ultramicroscopy 184, 177–187 (2018).

[91]K. Song, L. Liu, D. Zhang, M. P. Hautzinger, S. Jin, and Y. Han, Adv. Energy Mater. 1904006 (2020).

[92]X. Li, L. Yin, Z. Lai, M. Wu, Y. Sheng, L. Zhang, Y. Sun, S. Chen, X. Li, J. Zhang, Y. Li, K. Liu, K. Wang, D. Yu, X. Bai, W. Mi, and P. Gao, Natl. Sci. Rev. 7, 755–762 (2020).

[93]W. Huang, J. S. Manser, P. V. Kamat, and S. Ptasinska, Chem. Mater. 28, 303–311 (2016).

[94]Y. Xue, Y. Shan, and H. Xu, J. Chem. Phys. 147, 124702 (2017).

[95]C. Toyoshima, H. Sasabe, and D. L. Stokes, Nature 362, 469–471 (1993).

[96]B. Huang, G. Kong, E. N. Esfahani, S. Chen, Q. Li, J. Yu, N. Xu, Y. Zhang, S. Xie, H. Wen, P. Gao, J. Zhao, and J. Li, NPJ Quantum Mater. 3, 30 (2018).

[97]B. Huang, Z. Liu, C. Wu, Y. Zhang, J. Zhao, X. Wang, and J. Li, "Polar or nonpolar? That is not the question for perovskite solar cells," J. Appl. Phys. (submitted) (2020).

05 September 2023 02:30:25

[98]B. Chen, T. Li, Q. Dong, E. Mosconi, J. Song, Z. Chen, Y. Deng, Y. Liu, S. Ducharme, A. Gruverman, F. D. Angelis, and J. Huang, Nat. Mater. **17**, 1020–1026 (2018).

[99]L. Shu, S. Ke, L. Fei, W. Huang, Z. Wang, J. Gong, X. Jiang, L. Wang, F. Li, and S. Lei, Nat. Mater. **19**, 1–5 (2020).

[100]C. Zhang, J. F. Fernando, K. L. Firestein, J. E. von Treifeldt, D. Siriwardena, X. Fang, and D. Golberg, APL Mater. **7**, 071110 (2019).

[101]M. Vara, L. T. Roling, X. Wang, A. O. Elnabawy, Z. D. Hood, M. Chi, M. Mavrikakis, and Y. Xia, ACS Nano **11**, 4571–4581 (2017).

[102]Y. Lu, W. Yin, K. Peng, K. Wang, Q. Hu, A. Selloni, F. Chen, L. Liu, and M. Sui, Nat. Commun. **9**, 2752 (2018).

[103]P. Gao, J. Britson, J. R. Jokisaari, C. T. Nelson, S. Baek, Y. Wang, C. Eom, L. Chen, and X. Pan, Nat. Commun. **4**, 2791 (2013).

[104]M. Li, B. Wang, H. Liu, Y. Huang, J. Zhang, X. Ma, K. Liu, D. Yu, Y. Chu, L. Chen, and P. Gao, Acta Mater. **171**, 184–189 (2019).

05 September 2023 02:30:25